

Laminar free-surface flow around emerging obstacles: Role of the obstacle elongation on the horseshoe vortex

Gaby Launay*, Emmanuel Mignot, Nicolas Rivière

University of Lyon, LMFA, INSA de Lyon, 20 Avenue A. Einstein, 69100 Villeurbanne, France

ARTICLE INFO

Article history:

Received 10 October 2018

Received in revised form 10 April 2019

Accepted 15 April 2019

Available online 18 April 2019

Keywords:

Flow around obstacles

Free-surface

Recirculation

HSV

Wake

PIV

ABSTRACT

An emerging rectangular obstacle placed in a laminar boundary layer developing under a free-surface generates three vortical structures: a horseshoe vortex (HSV) in front of the obstacle, a wake downstream and two lateral recirculation zones at its sides. The present work investigates, through PIV measurements, the effect of the obstacle elongation (length over width ratio L/W) on the HSV, which is partly indirect through the modification of the two other vortical structures. Horizontal velocity fields in the near-bottom region show that an increase of the obstacle elongation leads to a higher adverse pressure gradient in front of the obstacle, and in consequence, to the longitudinal extension of the HSV. This modification of geometry, in turn, impacts the vortex dynamics of the HSV. On top of that, maps of spectra and oscillation direction obtained from velocity fields indicate that each of the three structures (HSV, wake and lateral recirculation zones) exhibits a proper oscillation frequency. As the oscillation associated to the wake is energetically dominant and is strong enough to travel upstream, it impacts the HSV dynamics for sufficiently short obstacles.

© 2019 Published by Elsevier Masson SAS.

1. Introduction

Flows around obstacles have been extensively studied since 1970 for their numerous applications in aerodynamics, thermal exchanges, turbo-machinery and hydraulics. These works investigated different obstacle shapes (cylinders, prisms, foils) and submergence (emerging, immersed or traversing). They showed that the horseshoe vortex (HSV) developing at the foot of the obstacle is a dominant structure that influences: (i) the bottom wall shear stress (impacting the scouring [1–3] and thermal exchanges [4]), (ii) the force exerted by the flow on the obstacle (impacting the efforts on the turbo-machinery blades or wings drag coefficients [5]) and (iii) the vortical structures released downstream (impacting the state of the downstream boundary layer). The evolution of the HSV characteristics with the obstacle and flow parameters was deeply studied [6–8]. However, the focus was put on prisms with square or round bases as obstacles, leaving aside the effect of the obstacle elongation on the HSV. Yet, in the previously cited domains of application, the obstacle can exhibit low (e.g. bridge piers) or high (e.g. cooling fins) elongations. Most of the studies moreover focused on the upstream (mainly the HSV) or on the downstream (which includes the wake) but rarely on the interactions between those two regions.

Studying the impact of the obstacle elongation on the HSV is, then, a first step to generalize the available results for square and round obstacles to elongated and shortened ones. In this context, the present study then focuses on the effect, on the HSV, of the streamwise length L of a rectangular prism of constant width W , emerging from a laminar, free-surface flow.

The interaction between a boundary layer – developing over a smooth wall and below a free surface – and a rectangular emerging obstacle leads to the appearance of three flow structures [9] (see Fig. 1): (i) a complex zone of recirculation in front of the obstacle, named “horseshoe vortex” (HSV). This recirculation is due to the adverse pressure gradient created by the obstacle, that causes the separation of the boundary layer. (ii) A large recirculation downstream of the obstacle, named “wake”. (iii) Additional lateral recirculations along each side of the obstacle, starting at the obstacle upstream vertical edges [9–11]. These recirculations are mingled with the wake for short obstacles and reattach on the obstacle sides for long enough obstacles. Still, Sau et al. [12] showed that for some configurations, these zones can appear only at a certain elevation above the bottom wall, because of the effect of the boundary layer.

The laminar HSV is composed of several vortices aligned from the boundary layer separation to the location of the obstacle face. Those vortices can exhibit complex dynamics [8,13] (motion, growth and diffusion) and interact with each other, leading in particular to vortex merging. Schwind [14] and Greco [15] implemented a qualitative typology for the dynamics of the HSV,

* Correspondence to: Smart Materials and Surfaces Laboratory, Northumbria University, Newcastle, United Kingdom.

E-mail addresses: gaby.launay@tutanota.com (G. Launay), emmanuel.mignot@insa-lyon.fr, nicolas.riviere@insa-lyon.fr (E. Mignot).

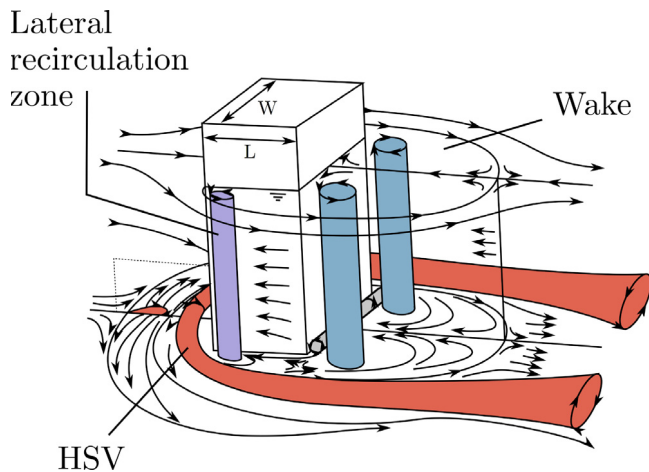


Fig. 1. Sketch of the flow around an obstacle emerging from a free-surface. The flow is expected to be three-dimensional in its lower part (which is not completely represented here), due to the boundary layer developing on the bottom wall.

based on flow visualizations. Extending this typology, Launay et al. [8] introduced a more quantitative typology, based on PIV measurements. This typology comprised 7 regimes, with five of them having a periodical behaviour. For high Reynolds numbers, the HSV is turbulent and exhibits a complex behaviour, notably featuring a bimodal dynamics [16]. The transition from laminar to turbulent HSV is intermittent and exhibits casual bursts of turbulence [17]. The evolution of the HSV general characteristics (size, number of vortices, vortex average position) with the flow parameters were summed up by Ballio et al. [6] for studies prior to 1995 and studied more recently by Lin et al. [13] and Launay et al. [8]. Nevertheless, none of these studies investigated the effect of the obstacle elongation.

For a rectangular obstacle (Fig. 1), the wake region starts at the downstream vertical edges of the obstacle and ends as the flow re-attaches. For a given range of Reynold numbers, the wake is known to exhibit a periodical behaviour characterized by vortex shedding. In the case of an obstacle placed upon a flat plate, the developing boundary layer modifies the wake oscillation characteristics and leads to Strouhal numbers [18] that vary with the vertical distance from the bottom wall [19]. Moreover, Chen and Jirka [20] showed that the transition from a periodical to a fully turbulent wake appears for higher Reynolds numbers in the case of an obstacle placed upon a solid wall ($Re_W = 3000$) than in the case of an infinitely high obstacle ($Re_W = 300$). Besides, these authors showed that a vertical flow confinement (due to a free-surface for example) stabilizes the wake further.

The question of the influence of the wake on the HSV is still open. Baker [21] observed that precluding the wake oscillation (by adding a plate in the plane of symmetry downstream to the obstacle) does not induce any modification in the HSV behaviour, and Ballio et al. [6], in their literature reviews, estimated that the HSV is only influenced by the shape and width of the upstream part of the obstacle. On the other hand, Baker [22] reported two oscillation frequencies in the HSV, the first one caused by the instability of the HSV vortices and the second one being a global oscillation, linked by Marakkos and Turner [23] to the wake oscillation. Paik and Sotiropoulos [24] performed numerical simulations featuring a HSV spatially close to a downstream recirculation. However, their configuration prevents the generation of high energy oscillations in the downstream recirculation, and thus, they did not observe any interactions between the two structures. In another configuration, Paik et al.

[25] studied numerically the interaction between the HSV and a wake generated by another obstacle placed upstream. To the authors knowledge, only two articles investigated the impact of the obstacle elongation L/W on the flow around. For immersed rectangular obstacles, Larousse et al. [9] studied the influence of the obstacle elongation L/W (in the range $[0.04, 1]$), keeping the obstacle height H equal to its length L . Their visualizations (Fig. 8 in [9]) indicate that the dimensionless distance between the boundary layer separation distance increases with the obstacle elongation L/W . Nevertheless, this effect is expected to be caused by the increasing obstacle height which results in a higher adverse pressure gradient upstream of the obstacle, and consequently a precocious boundary layer separation. Younis et al. [26] studied the evolution of the HSV for three immersed obstacles with varying elongations and shapes and did not report any modification of the HSV properties. Their configuration however differs from the present configuration, as the rounded shape of their obstacles prohibits the development of the wake and lateral recirculation zones. In summary, no conclusion can be drawn on the isolated effect of the elongation L/W of a rectangular obstacle on the HSV extension and dynamics.

The aim of the present work is then, for a given laminar free-surface flow interacting with an emerging rectangular obstacle, to : (i) measure the influence of the obstacle elongation (L/W) on the three main structures of the flow (HSV, lateral recirculation zones and wake), and (ii) identify their mutual interactions.

2. Experimental method

The flow velocity fields are measured using 2D particle image velocimetry (PIV) in the upstream vertical plane of symmetry ($z = 0$) and in the horizontal plane around the obstacle, near the bottom wall ($y \approx 2$ mm, i.e. 3.3% of the approaching water depth). These measurements permit to characterize the HSV dynamics (vertical planes) and the interactions between the three flow structures (horizontal planes). Note however that the lateral recirculation zones and the wake are known to be three-dimensional near the bottom wall. For this reason, horizontal measurements of these structures in the vicinity of the bottom wall do not allow to access their complete characteristics.

A 532 nm, 4W continuous laser with a Powell lens is used to illuminate 10 μ m hollow glass spheres (density $\rho = 1.1$) included as tracers in the flow. Images of the displacement of these particles are recorded with a mono-chromatic, 12bit, 2048 \times 1088 pixels camera, at a frequency of 2 Hz (more than 20 times the highest frequency exhibited by the flow) more than 20 periods of HSV and wake oscillations. Image treatments and PIV computations are realized using DaVis software (Lavis) and further velocity field treatments are performed using Python (Python Software Foundation). Image treatments include ortho-rectification, background removal, intensity capping and moving average. PIV computations are performed using cross-correlation with 50% overlapping and adaptive interrogation windows (sizes from 64 to 16 pixels), leading to a spatial resolution of approximately 0.2 mm per pixel.

The accuracy of the velocity measurements is of great importance for flow dynamics study. For this reason, a special care is taken in reducing the measurement uncertainties. The Stokes number associated to the tracers is $St_p = 0.04$ for the maximum measured velocity. According to Tropea et al. [27], this results in an uncertainty associated to the particles advection of less than $\pm 1\%$. Uncertainty on the measured velocity ($\pm 2\%$) is estimated using the method from Wieneke [28]. The reproducibility of the flow generation procedure and of the PIV measurement is ascertained by the good agreement between vertical and horizontal measurements regarding (i) the boundary layer separation position, (ii) the HSV characteristic frequency and (iii) the velocity

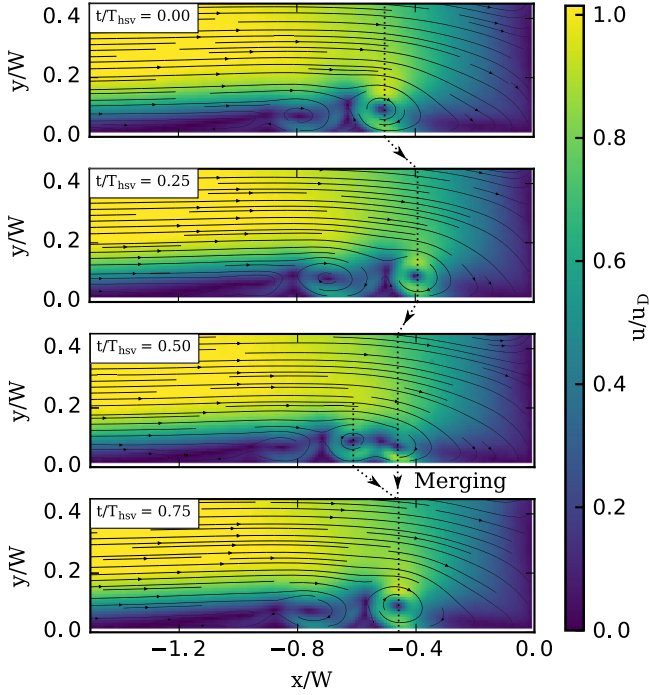


Fig. 2. Successive instantaneous velocity fields (streamlines and velocity magnitude) in the vertical plane of symmetry for $L/W = 6$. The period associated to the HSV dynamics is $T_{hsv} = 38.5$ s. The obstacle face is located at $x/W = 0$.

along x on the common line at $y = 2$ mm and $z = 0$ (relative difference at most of 2%). PIV measurements at the position of the obstacle, performed before introducing it, reveal that the boundary layer shape factor $H = 2.64$ is very close to the value of 2.59 expected for a laminar Blasius boundary layer. The boundary layer thickness, however, slightly differs from the Blasius solution ($\delta/\delta_{blasius} = 0.82$). Launay et al. [8] showed that this effect was due to the confinement of the free-surface. This confinement can also explain the existence of a laminar boundary layer for such high Reynolds number ($Re_h = 4800$, see below).

To investigate the interactions between the oscillating behaviour of the three flow structures, a flow regime exhibiting an oscillating HSV and an oscillating wake is selected. In this flow configuration, the dynamics of the HSV belongs to flow type “amalgamating” in the typology of Greco [15] and “merging” in the typology from Launay et al. [8]. The associated dimensional parameters are the water depth $h = 0.06$ m, the boundary layer thickness before introducing the obstacle $\delta = 0.022$ m, the obstacle width $W = 0.1$ m and the mean velocity $u_D = 0.02$ m s⁻¹. The associated dimensionless parameters are: $Re_h = 4hu_D/\nu = 4800$, $h/\delta = 2.73$ and $W/h = 1.67$, with ν the water kinematic viscosity. The obstacle length is varied from $L = 0.04$ m to $L = 0.6$ m, leading to dimensionless obstacle elongations of $L/W \in [0.4, 0.74, 1, 1.25, 1.5, 2, 4, 6]$. Propagating the uncertainties related to the device setup (on h , u_D , W , L and on the ambient temperature) to the dimensionless parameters give an uncertainty between 1% and 3.5% on L/W , of 10% on Re_h , of 3% on W/h , and of 3.5% on h/δ .

3. Results

This section discusses the influence of the obstacle elongation L/W on the HSV shape and dynamics (Section 3.1) and on the characteristic oscillation frequencies (Section 3.2), while its final part is dedicated to the impact of the wake oscillation on the HSV (Section 3.3).

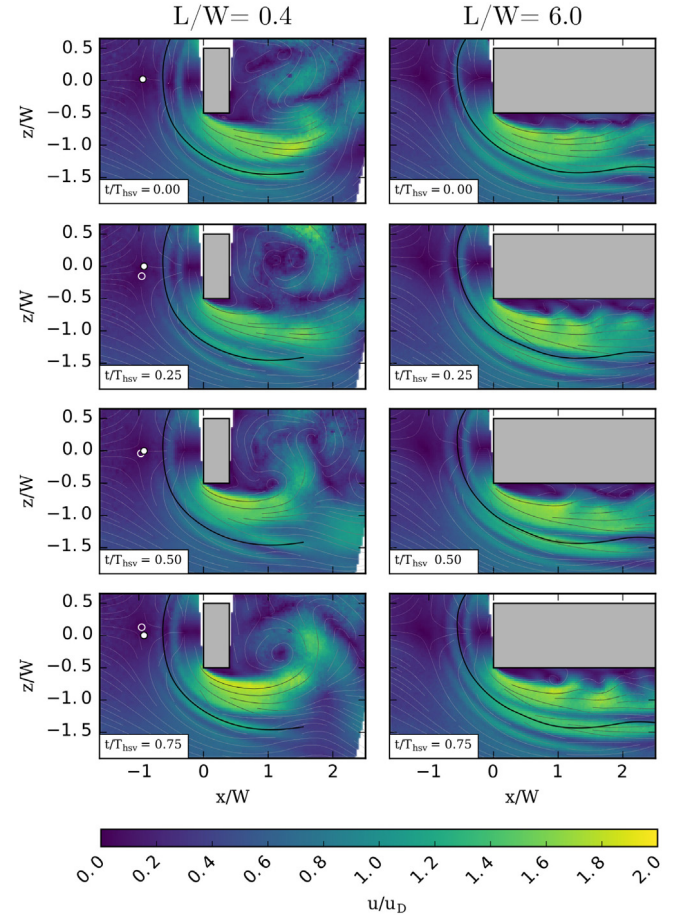


Fig. 3. Successive Instantaneous fields (streamlines and velocity magnitude) in the horizontal plane near the bottom wall for $L/W = 0.4$ (left, with $T_{hsv} = 39.79$ s) and $L/W = 6.0$ (right, with $T_{hsv} = 38.5$ s). The black line corresponds to a vortex filament position at $t/T_{hsv} = 0$. For $L/W = 0.4$, the white open circle represents the position of the saddle point in the boundary layer separation line at $t/T_{hsv} = 0$ and the white filled circles correspond to its position at the considered times.

3.1. Impact of the obstacle elongation on the HSV

Fig. 2 presents the structure and periodical dynamics of the vortices composing the HSV for a long obstacle ($L/W = 6$). A period consists of a phase of vortex advection (from $t/T_{hsv} = 0$ to 0.5 in Fig. 2) followed by a vortex merging (between $t/T_{hsv} = 0.5$ and $t/T_{hsv} = 0.75$). Besides, measurements in the horizontal plane near the bottom wall (Fig. 3) reveal that the vortices roll around the obstacle and remain visible until they leave the measurement zone (for elongated obstacles), such as $L/W = 6$ or until they are destroyed by the wake recirculation (for short obstacles, such as $L/W = 0.4$).

Fig. 4 presents the evolution, with L/W , of one of the main property of the HSV: the distance λ between the boundary layer separation position upstream of the obstacle and a point at $W/2$ downstream from the obstacle face (as proposed by Ballio et al. [6]). λ is extracted from measurements in the vertical plane of symmetry (e.g. Fig. 2) by linearly extrapolating the zero-velocity line down to the bottom wall. While the HSV exhibits a complex dynamics, the separation position does not change in time (as also observed by Launay et al. [8] for HSV in such regime). As the uncertainty on the velocity is estimated small ($\pm 2\%$), the uncertainty on λ (± 0.33 mm) can be estimated from the velocity field spatial resolution $\Delta y = 0.2$ mm and the extrapolation

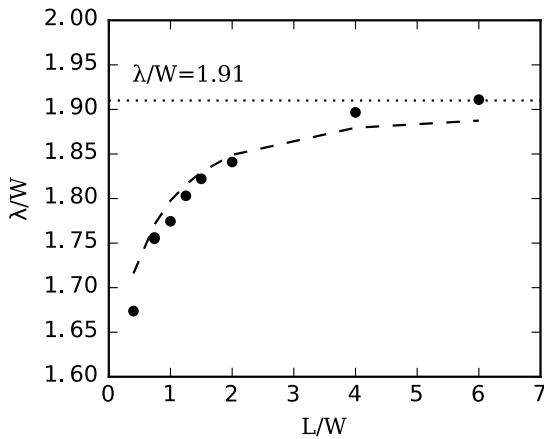


Fig. 4. Boundary layer separation distance λ evolution as a function of L/W . Black circles : λ/W values measured in the vertical plane of symmetry (as in Fig. 2). Dashed lines : estimated values of the separation distance λ_{cp} , based on potential flow computations (as in Fig. 5a) and Eq. (1) with $k = 0.00113$. Horizontal dotted line : empirical correlation from Launay et al. [8] for long obstacles ($\lambda/W = 1.91$). Uncertainties on λ associated to the PIV measurement can be estimated to be of $\Delta\lambda/W \pm 3.3 \times 10^{-3}$.

properties. Fig. 4 indicates that λ increases with L/W but tends to stabilize to a constant value after a threshold value of $L/W = 4$, in agreement with the empirical correlation from Launay et al. [8] for long obstacles. Younis et al. [26] rather reported a value of $L/W \approx 1$ for this threshold. In order to shed the light on this threshold value, a simple model based on the potential flow theory is presented herein. The streamwise pressure gradient $\frac{\partial p}{\partial x}$ in the vertical plane of symmetry upstream of the obstacle is estimated using potential flow computation (Fig. 5) for each obstacle elongation.

As this pressure gradient is at the origin of the boundary layer separation, one can get a rough estimate of the distance between the obstacle and the boundary layer separation λ_{cp} by choosing an adequate critical value k for the pressure coefficient gradient :

$$\frac{\partial C_p}{\partial x} (x = -\lambda_{cp}) = k \quad (1)$$

with $C_p = p/(\rho u_D^2/2)$ the pressure coefficient. Fitting the value of k on the experimental data (least square method) results in $k = 0.00113$ and the dashed line in Fig. 4. The good agreement between the measurements and the fit of Eq. (1) indicates that the modification of λ is strongly linked to the modification of the pressure gradient. Taking into account the lateral recirculation zones as part of the obstacle in the potential flow computation (as illustrated by Fig. 5b) increases the adverse pressure gradient upstream of the obstacle (not shown here). This leads to a different fitted value of k , but does not improve the agreement for the boundary layer separation distance. For $L/W = 1$, the value of $\lambda/W = 1.77$ (see Fig. 4) can be compared to the value obtained by Larousse et al. [9] of $\lambda/W = 1.3$ (once adapted using the method from Ballio et al. [6]). The discrepancy between those values is due to the difference of configuration (emerging obstacle in the present study, and immersed obstacle for Larousse et al. [9]), which causes a modification of the down-flow strength, as reported by Sadeque et al. [29].

The evolution of λ with L/W is associated to an evolution of the HSV vortices dynamics, as illustrated on Fig. 6 by mean vortex trajectories measured in the vertical plane of symmetry. Mean trajectories are obtained by averaging the trajectories of successive vortices, allowing to visualize synthetically the vortices main paths. The mean trajectories can be seen as a synthetic

representation of the dynamics exhibited by the HSV: vortices appear in the upstream part of the HSV, are advected downstream, and disappear by merging with the following vortex. The HSV dynamics is slightly modified with the increase of the obstacle elongation. As L/W increases, the main (downstream-most) vortex (i) travels further downstream before going back to merge with the secondary vortex, and (ii) is no longer detected as it goes back upstream towards the secondary vortex, indicating that its circulation reduces drastically.

Two major conclusions can finally be drawn regarding the effect of the obstacle elongation: (i) it increases the separation distance of the HSV λ through the modification of the adverse pressure gradient generated by the obstacle, and (ii) this increase of the HSV streamwise extension affects the vortex dynamics.

3.2. Characteristic frequencies of the three flow structures

Each of the three flow structures (HSV, lateral recirculation zones and wake) exhibits a periodical behaviour, schematized on Fig. 7: (i) The HSV is in a periodic regime, characterized by a frequency linked to the vortex motion (see Figs. 2 and 6), the resulting oscillation is oriented in the streamwise direction (along x) in the plane of symmetry. (ii) The shear layer along the separating streamline of the lateral recirculation zones can generate vortices [11] (as seen on Fig. 3 for $L/W = 6$) and thus create a periodic oscillation perpendicular to the shear layer. (iii) The wake generates a periodic oscillation in the transverse direction (along z) due to the alternative shedding of vortices (visible for $L/W = 0.4$ at $t/t_{HSV} = 0.75$ on Fig. 3). Because the obstacle elongation affects the overall flow topology (see Fig. 8), the periodic oscillations of the three flow structures are also expected to evolve with L/W .

Velocity spectra are gathered at the locations associated with the three flow structures (S_{HSV} , S_{lrz} , S_{wake} on Fig. 7) and are plotted for $L/W = 1.25$ on Fig. 9. These spectra allow to identify the characteristic frequencies associated with each of the three periodic oscillations. The spectral densities indicate a peak frequency of $f_{wake} = 0.016$ Hz at S_{wake} and a peak frequency of $f_{HSV} = 0.025$ Hz at S_{HSV} . The wake oscillation is more energetic than the HSV oscillation (considering the integrals of the spectral density peaks). For S_{lrz} , the spectral density shows a peak frequency at f_{wake} , and a smaller peak at $f_{lrz} = 0.167$ Hz, which corresponds to the qualitatively observed vortex shedding frequency in the lateral recirculation zone. Based on scaling arguments and experiments, Lander et al. [11] predict a ratio $f_{lrz}/f_{wake} = 0.18Re_W^{0.6} = 17.21$, which must be divided by 2 in the downstream part of the recirculation zone (for $x/L > 0.2$) because of vortex merging. The present frequency ratio measured at $x/L = 0.25$ is $f_{lrz}/f_{wake} = 10.48$ and can be considered in satisfactory agreement with $0.18Re_W^{0.6}/2 = 8.61$.

The same procedure repeated with several values of L/W results in the evolution of the characteristic frequencies of the three oscillation for increasing obstacle elongations (Fig. 10). HSV peak frequencies (measured at S_{HSV}) do not vary significantly with L/W and are in good agreement with the correlation from Launay et al. [8] ($f_{HSV} = 211u_D^{2.33}$). Wake peak frequencies (measured at S_{wake}) give a Strouhal number based on the obstacle width $St_W = f_{wake}W/u_D \in [0.08, 0.10]$, in agreement with the Strouhal number of 0.08 found by Okajima [18] for immersed rectangular obstacles. The intensity of the wake oscillation decreases rapidly from $L/W = 0.4$ to $L/W = 1.5$ (white squares on Fig. 11), reaching a very low value for $L/W > 2$. For $L/W < 1.25$, the lateral recirculation zones do not show any peak frequency (at S_{lrz}), the shear layer being too short to shed vortices. For higher values of L/W , the lateral recirculation zones characteristic frequency remains relatively constant, at $f_{lrz} \approx 0.165$ Hz.

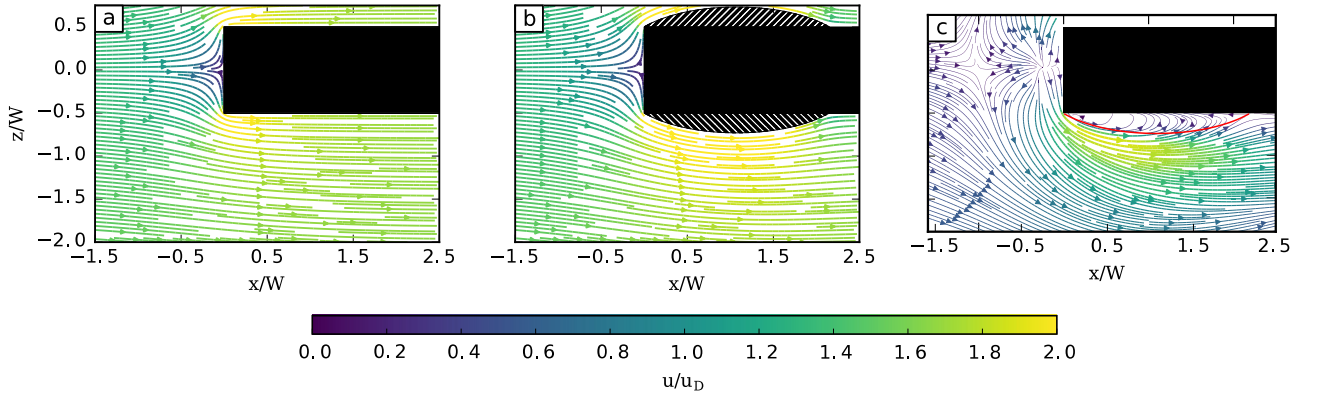


Fig. 5. Potential flow computation on a 2D horizontal flow around a rectangular obstacle. (a) Velocity fields for $L/W = 6$. (b) Same as (a) but for an obstacle adapted to encompass the measured lateral recirculation zones. (c) measured velocity field for $L/W = 6$. The red line highlights one of the lateral recirculation zone. (For interpretation of the references to colour in this figure legend, the reader is referred to the web version of this article.)

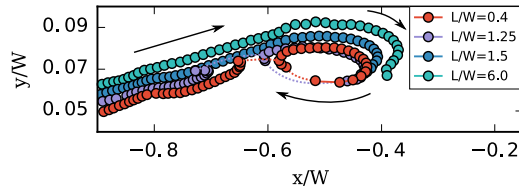


Fig. 6. Mean trajectories of vortex centres in the vertical plane of symmetry for increasing values of L/W . For clarity, mean trajectories are not presented in an orthonormal referential but rather stretched along the y axis. Black arrows indicate the vortices direction of motion. The vortex extraction method being unable to detect vortices advected at high velocities, the trajectories gaps are filled using the residual vorticity [30] as a vortex criterion (dotted lines). (For interpretation of the references to colour in this figure legend, the reader is referred to the web version of this article.)

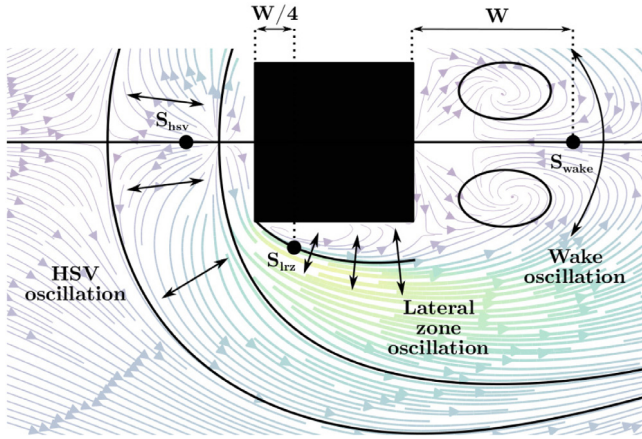


Fig. 7. Schematic diagram illustrating the three structures (HSV, lateral recirculation zone and wake) oscillation directions. S_{HSV} , S_{Lrz} and S_{wake} are the locations where the three structures characteristic frequencies are measured (see Fig. 9).

To conclude, each of the three flow structures (HSV, wake and lateral recirculation zones) exhibits a proper characteristic frequency which does not evolve much with W/L . The increasing values of λ with increasing elongation is thus not related to a change of oscillation frequency.

3.3. Interactions between the wake and the HSV

The wake oscillation can, in the case of short obstacles, propagate upstream and impact the dynamics of the lateral zones of

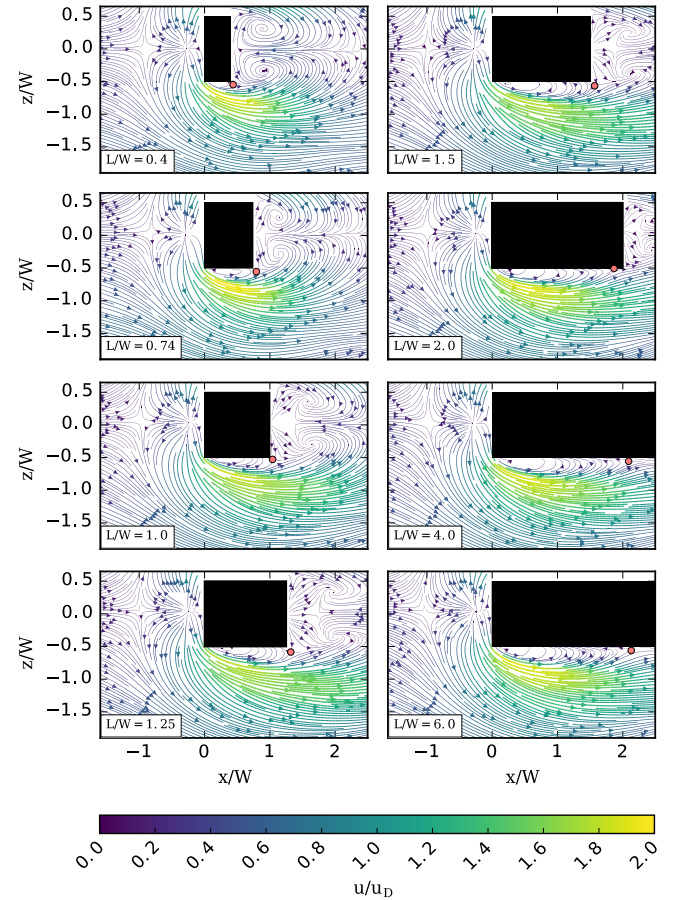


Fig. 8. Mean flow evolution in the horizontal plane near the bottom wall for increasing values of L/W . Red circles represent the saddle points defining the end of the lateral recirculation zone.

recirculation and the HSV. This effect is visible on the boundary layer separation saddle point position, which spatially oscillates in front of the obstacle along the z axis (see white symbols for $L/W = 0.4$ in Fig. 3) at a frequency equal to 0.016 Hz. This frequency differs significantly from the HSV peak oscillation frequency $f_{HSV} = 0.025$ Hz but equals the wake oscillation frequency $f_{wake} = 0.016$ Hz (see Fig. 10). The transverse oscillation amplitude of this saddle point (A_z) is plotted on Fig. 11 as a function of L/W , and shows a non-negligible value (one third of the obstacle width) for $L/W = 0.4$ and a rapid decrease for larger

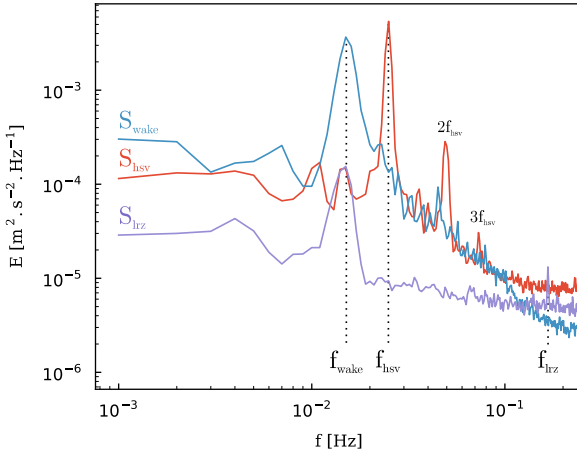


Fig. 9. Velocity power spectral density (on v_x for the HSV and on v_z for the wake and the lateral recirculation zone) for $L/W = 1.25$. Red curve stands for the HSV (point S_{hsv}), purple curve for the lateral recirculation zone (point S_{lrz}), and blue curve for the wake (point S_{wake}). Power spectral densities are computed using the method from Welch [31], with a window of 1000s (500 points). Dashed vertical lines indicate peak frequencies. Uncertainty on the peak frequencies ($\pm 0.7\%$) is estimated from the resolution (in Hz) of the spectrum.

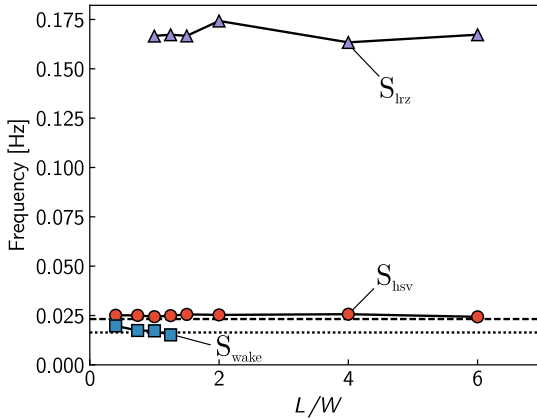


Fig. 10. Evolution of the three main structures characteristic frequencies with L/W . Red circles: HSV, Blue squares: wake, and purple triangles: lateral recirculation zone. Dotted line represents the wake frequency obtained from a Strouhal number based on the water level of 0.08 [18]. Dashed line represents the HSV frequency obtained using the correlation from Launay et al. [8].

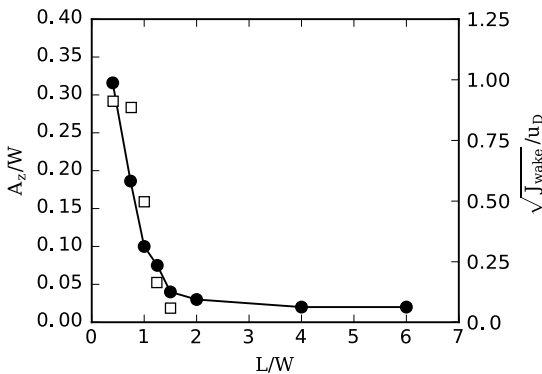


Fig. 11. Filled circles: Oscillation amplitude of the separation point position along z (A_z). White squares: Dimensionless oscillation intensity of the wake $\sqrt{J_{wake}}/u_D$, with J_{wake} computed by integrating the spectrum around f_{wake} . Uncertainties on A_z associated to the PIV measurement can be estimated to be of $\Delta A_z/W \pm 4 \times 10^{-3}$.

L/W values, becoming negligible for $L/W > 2$. This evolution can be explained by the combined effect, as L/W increases, of the decreasing wake oscillation intensity (squares on Fig. 11) and of the increasing distance separating the wake and the HSV.

Fig. 12 shows the spatial distribution in the horizontal plane of the oscillation intensity (colours) and direction (rod orientation) for the two main frequencies f_{hsv} and f_{wake} and for $L/W = 0.4$.

Those oscillation maps are obtained using the following methodology : (i) For each measurement point, the spectral densities (S_x and S_z) and the associated phase spectra (Φ_x and Φ_z) are obtained by FFT (Fast Fourier Transform) for the two horizontal velocity components v_x and v_z . (ii) Oscillation specific energies (J_x and J_z) are obtained for each points by integrating the spectral density (as in Fig. 9) on a frequency interval ($\Delta f = 0.002$ Hz) around each selected frequency. (iii) The corresponding phases (ϕ_x and ϕ_z) are obtained on the phase spectra at the selected frequencies. (iv) The phase shift between the two horizontal velocity components oscillations is calculated as : $\phi = \phi_x - \phi_z$. (v) The specific energy associated with the oscillation is computed as : $J = (J_x^2 + J_z^2)^{0.5}$. And finally, (vi) the main oscillation direction vector \vec{e} is computed as :

$$\vec{e} = \frac{1}{J} \begin{bmatrix} J_x \text{sign}(\cos \phi) \\ J_z \end{bmatrix} \quad (2)$$

As expected, for frequency f_{hsv} (Fig. 12a), the HSV main oscillation is aligned along x in the upstream symmetry plane. As the HSV rolls around the obstacle, and until $x/W = 0.5$, its main oscillation direction remains roughly oriented toward the obstacle centre. Further downstream ($x/W > 0.5$), the HSV oscillation intensity decreases, due to its interaction with the wake. The double branch formed by the HSV at $x/W \approx 1$ seems to be an effect of the HSV flapping along the z axis caused by the wake oscillation (visible on Fig. 3 for $L/W = 0.4$). It is unlikely that the important oscillation intensities at frequency f_{hsv} in the wake are the result of the HSV oscillation and they are more probably due to the wake frequency spreading (visible on the wake velocity spectrum in Fig. 9), the wake carrying a non-negligible quantity of proper energy at the frequency f_{hsv} . Finally, the small oscillation intensities upstream from the obstacle area in Fig. 12a indicate that the HSV influence does not travel further upstream than $x/W = -0.75$.

Regarding frequency f_{wake} (Fig. 12b), oscillation intensities are globally more energetic than for f_{hsv} . As expected, the maximum intensity appears in the wake region, along the transverse direction (along z). This strong oscillation zone bypasses the obstacle toward upstream, passing through : (i) the lateral recirculation zone (where the main oscillation direction is streamwise), the influence of the wake on this zone having already been observed on the spectral density (Fig. 9) for $L/W = 1.25$ at point S_{lrz} , (ii) the HSV zone, where the oscillation direction is transverse (along z), the wake being at the origin of the transverse oscillation of the boundary layer separation point position (already reported on Fig. 3 for $L/W = 0.4$ and Fig. 11). In conclusion, for short obstacles ($L/W < 2$), the wake generates a global circular oscillation, centred around a point in the obstacle (as indicated by grey-headed arrows on Fig. 12b) that is modified by the impact of the HSV (black arrows in Fig. 12b).

4. Conclusion

One major conclusion of this work is that each of the three flow structures (HSV, lateral recirculation zones and wake) exhibits a proper characteristic frequency, revealing that they all generate perturbations independently. This indicates that none of the three structures results from the perturbation generated by another one. Notably, the wake oscillation, despite its high

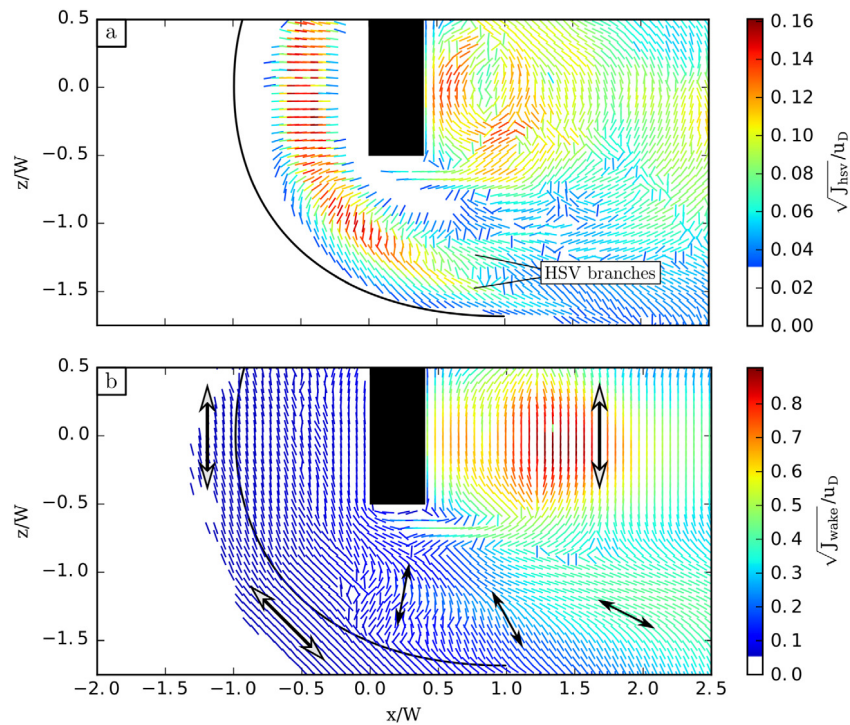


Fig. 12. Map of the main oscillation directions (rods) and intensities (colours) in the horizontal plane for $L/W = 0.4$. (a) For the frequency associated to the HSV : $f_{HSV} = 0.025$ Hz. (b) For the frequency associated to the wake : $f_{wake} = 0.016$ Hz. Black line : boundary layer separation line (delimiting the HSV). Grey-headed arrows indicate the direction of oscillation due to the wake. Black-headed arrows indicate the oscillation disturbances due to the HSV. It is to be noted that the colour map differs for (a) and (b). (For interpretation of the references to colour in this figure legend, the reader is referred to the web version of this article.)

intensity, is not responsible for the HSV vortices dynamics (in the streamwise direction) or of the vortex shedding in the lateral recirculation zones. The impact of the obstacle elongation on the HSV can be summarized in 4 points:

- (i) As shown by potential flow computations, the increasing elongation of the obstacle causes a stronger adverse pressure gradient, leading to a precocious separation of the boundary layer.
- (ii) This increase of the boundary layer separation distance affects the HSV dynamics, and affects its vortices motion.
- (iii) For short obstacles, the wake vortex shedding disturbances travel upstream and impact the HSV, leading to a global transverse oscillation. For long obstacles ($L/W > 2$), the wake has no effect on the HSV (Fig. 11).
- (iv) The HSV coherency is rapidly damped (by the wake for short obstacles and by the lateral recirculation zones for long obstacles) as it wraps around the obstacle towards downstream.

Both the modification of the boundary layer separation distance and of the transverse oscillation of the HSV (provoked by the wake) should affect the bottom wall shear stress distribution. Consequently, the scouring starting point, as well as the final bed topography may differ for two obstacles with different elongations. For the same reason, the thermal exchanges through the bottom wall should be affected by the obstacle elongation. The obstacle elongation also affects the flow structures oscillation intensities, which would impact the oscillatory behaviour in the case of turbo-machinery blades. Note however that this study only investigated the impact of the obstacle elongation for one flow configuration. The other parameters of the flow (Re_h , h/δ , W/h and Fr , see Launay et al. [8]) are also expected to affect the flow properties. Additional work would be required to properly characterize the impact of these parameters on the wake/HSV interactions.

References

- [1] S. Dey, S.K. Bose, Bed shear in equilibrium scour around a circular cylinder embedded in a loose bed, *Appl. Math. Model.* 18 (5) (1994) 265–273.
- [2] A. Roulund, B.M. Sumer, J. Fredsoe, J. Michelsen, Numerical and experimental investigation of flow and scour around a circular pile, *J. Fluid Mech.* 534 (2005) 351–401, <http://dx.doi.org/10.1017/S002112005004507>.
- [3] C. Escarriaza, F. Sotiropoulos, Initial stages of erosion and bed form development in a turbulent flow around a cylindrical pier, *J. Geophys. Res.* 116 (F3) (2011).
- [4] D.R. Sabatino, C.R. Smith, Boundary layer influence on the unsteady horseshoe vortex flow and surface heat transfer, *J. Turbomach.* 131 (1) (2008) <http://dx.doi.org/10.1115/1.2813001>, 011015–011015.
- [5] P.E. Roach, J.T. Turner, Secondary loss generation by gas turbine support struts, *Int. J. Heat Fluid Flow* 6 (2) (1985) 79–88.
- [6] F. Ballio, C. Bettoni, S. Franzetti, A survey of time-averaged characteristics of laminar and turbulent horseshoe vortices, *J. Fluids Eng.* 120 (2) (1998) 233–242, <http://dx.doi.org/10.1115/1.2820639>.
- [7] R.L. Simpson, Junction flows, *Annu. Rev. Fluid Mech.* 33 (1) (2001) 415–443, <http://dx.doi.org/10.1146/annurev.fluid.33.1.415>.
- [8] G. Launay, E. Mignot, N. Riviere, R. Perkins, An experimental investigation of the laminar horseshoe vortex around an emerging obstacle, *J. Fluid Mech.* 830 (2017) 257–299, <http://dx.doi.org/10.1017/jfm.2017.582>, ISSN: 0022-1120, 1469-7645.
- [9] A. Larousse, R. Martinuzzi, C. Tropea, Flow around surface-mounted, three-dimensional obstacles, in: F. Durst, R. Friedrich, B.E. Launder, F.W. Schmidt, U. Schumann, J.H. Whitelaw (Eds.), *Turbulent Shear Flows 8: Selected Papers from the Eighth International Symposium on Turbulent Shear Flows*, Munich, Germany, September 9 – 11, 1991, Springer Berlin Heidelberg, 1993, pp. 127–139, ISBN: 978-3-642-77676-2 978-3-642-77674-8.
- [10] J.-Y. Hwang, K.-S. Yang, Numerical study of vortical structures around a wall-mounted cubic obstacle in channel flow, *Phys. Fluids* 16 (7) (2004) 2382–2394, <http://dx.doi.org/10.1063/1.1736675>.
- [11] D.C. Lander, D.M. Moore, C.W. Letchford, M. Amitay, Scaling of square-prism shear layers, *J. Fluid Mech.* 849 (2018) 1096–1119, <http://dx.doi.org/10.1017/jfm.2018.443>, ISSN: 0022-1120, 1469-7645.
- [12] A. Sau, R.R. Hwang, T.W.H. Sheu, W.C. Yang, Interaction of trailing vortices in the wake of a wall-mounted rectangular cylinder, *Phys. Rev. E* 68 (2003) 056303.
- [13] C. Lin, T.C. Ho, S. Dey, Characteristics of steady horseshoe vortex system near junction of square cylinder and base plate, *J. Eng. Mech.* 134 (2) (2008) 184–197, [http://dx.doi.org/10.1061/\(ASCE\)0733-9399\(2008\)134:2\(184\)](http://dx.doi.org/10.1061/(ASCE)0733-9399(2008)134:2(184)).

- [14] R.G. Schwind, The three dimensional boundary layer near a strut (Ph.D. thesis), Massachusetts Institute of Technology, 1962.
- [15] J. Greco, The flow structure in the vicinity of a cylinder-flat plate junction: Flow regimes, periodicity, and vortex interactions (Ph.D. thesis), Department of Mechanical Engineering and Mechanics, Lehigh University, 1990.
- [16] J. Paik, C. Escauriaza, F. Sotiropoulos, On the bimodal dynamics of the turbulent horseshoe vortex system in a wing-body junction, *Phys. Fluids* 19 (4) (2007) 045107.
- [17] C. Escauriaza, F. Sotiropoulos, Reynolds number effects on the coherent dynamics of the turbulent horseshoe vortex system, *Flow Turbul. Combust.* 86 (2) (2011) 231–262.
- [18] A. Okajima, Strouhal numbers of rectangular cylinders, *J. Fluid Mech.* 123 (1982) 379–398.
- [19] B. Dargahi, The turbulent flow field around a circular cylinder, *Exp. Fluids* 8 (1989) 1–12, <http://dx.doi.org/10.1007/BF00203058>.
- [20] D. Chen, G.H. Jirka, Experimental study of plane turbulent wakes in a shallow water layer, *Fluid Dyn. Res.* 16 (1) (1995) 11–41.
- [21] C.J. Baker, The laminar horseshoe vortex, *J. Fluid Mech.* 95 (1978) 347.
- [22] C.J. Baker, The oscillation of horseshoe vortex systems, *ASME Trans. J. Fluids Eng.* 113 (1991) 489–495.
- [23] K. Marakkos, J.T. Turner, Vortex generation in the cross-flow around a cylinder attached to an end-wall, in: *Colour and Design in the natural and man-made worlds*, *Opt. Laser Technol.* 38 (2006) 277–285, <http://dx.doi.org/10.1016/j.optlastec.2005.06.014>.
- [24] J. Paik, F. Sotiropoulos, Coherent structure dynamics upstream of a long rectangular block at the side of a large aspect ratio channel, *Phys. Fluids* 17 (11) (2005) 115104.
- [25] J. Paik, F. Sotiropoulos, F. Porté-Agel, Detached eddy simulation of flow around two wall-mounted cubes in tandem, *Int. J. Heat Fluid Flow* 30 (2) (2009) 286–305.
- [26] M.Y. Younis, H. Zhang, B. Hu, Z. Muhammad, S. Mehmood, Investigation of different aspects of laminar horseshoe vortex system using PIV, *J. Mech. Sci. Technol.* 28 (2) (2014) 527–537, <http://dx.doi.org/10.1007/s12206-013-1120-9>.
- [27] C. Tropea, A. Yarin, J. Foss (Eds.), *Springer Handbook of Experimental Fluid Mechanics*, 2007 ed., Springer, 2007.
- [28] B. Wieneke, PIV Uncertainty quantification from correlation statistics, *Meas. Sci. Technol.* 26 (7) (2015) 074002, <http://dx.doi.org/10.1088/0957-0233/26/7/074002>.
- [29] M. Sadeque, N. Rajaratnam, M. Loewen, Flow around cylinders in open channels, *J. Eng. Mech.* 134 (1) (2008) 60–71, [http://dx.doi.org/10.1061/\(ASCE\)0733-9399\(2008\)134:1\(60\)](http://dx.doi.org/10.1061/(ASCE)0733-9399(2008)134:1(60)).
- [30] V. Kolář, Vortex identification: new requirements and limitations, in: Including Special Issue of Conference on Modelling Fluid Flow (CMFF'06), Budapest 13th Event of the International Conference Series in Fluid Flow Technologies: Conference on Modelling Fluid Flow, *Int. J. Heat Fluid Flow* 28 (4) (2007) 638–652, <http://dx.doi.org/10.1016/j.ijheatfluidflow.2007.03.004>.
- [31] P. Welch, The use of fast fourier transform for the estimation of power spectra: a method based on time averaging over short, modified periodograms, *IEEE Trans. Audio Electroacoust.* 15 (2) (1967) 70–73.